nature communications

Article

https://doi.org/10.1038/s41467-026-70680-0

Implantable soft bladder-machine interface for neurogenic bladder dysfunction

Received: 1 July 2025

Accepted: 26 February 2026

Published online: 16 March 2026

Check for updates

Hanfei Li[1,2,3,12], Shuai Wang[4,5,12], Qianhengyuan Yu[1], Hang Zhao[1], Zhuochao Tang[6], Linchen Lv[4,5], Fei Han[1], Ruofan Yang[1], Yang Zhao[1], Zhuojia Fu[7], Benkang Shi[4,5], Guanglin Li[1], Changxian Wang[8], Jie Zhang[8], Kaikai Song[2,13] ✉, Yan Li[4,5,13] ✉ & Zhiyuan Liu[1,9,10,11,13] ✉

Neurogenic bladder dysfunction impairs bladder sensation and contraction, causing severe renal complications. The bladder's large isotropic expansion hinders the development of implantable bioelectronic devices for monitoring and electrical stimulation. Addressing this, we report an implantable soft bladder-machine interface (BdMI) that integrates seamlessly with the bladder, providing monitoring and electrical stimulation. This BdMI features a conductive thin film capable of keeping functions under isotropic stretch up to 800%, created without the complex pre-stretching of its elastic substrate. We elucidate its stretchability mechanism and validate the BdMI in rat models, which enables simultaneous intravesical pressure detection, detrusor electromyographic monitoring, and electrical stimulation therapy. Implanted for 7 days, the BdMI operates efficiently and markedly reduces involuntary bladder contraction frequency post-stimulation. These findings validate the potential of BdMI in offering real-time, physiological feedback and electrical stimulation-based regulation for neurogenic bladder pathologies, marking a significant advancement in the field.

Bladder-related pathologies like neurogenic lower urinary tract dysfunction (NLUTD), refractory overactive bladder, and detrusor-sphincter dyssynergia affect over 200 million people globally, leading to increased morbidity and mortality[1–3]. For instance, 80% of the annual 250,000–500,000 spinal cord injury (SCI) patients develop NLUTD within 2 years post-injury[4–10]. Without proper management, this can jeopardize the upper urinary tract, resulting in vesicoureteral reflux, hydronephrosis, and potentially renal impairment or end-stage renal disease, posing life-threatening risks[11,12]. Furthermore, most patients lack bladder capacity perception, complicating patient care. This underlines the need for a bladder-machine interface (BdMI) for effective bladder monitoring and regulation. While past research has investigated single-mode acute and in-vitro bladder monitoring, and electrical stimulation of the bladder wall has shown potential in mitigating SCI symptoms[13–19], the development of a soft thin-film, long-term implantable monitoring and electrical stimulation system

[1]Neural Engineering Centre, Shenzhen Institutes of Advanced Technology, Chinese Academy of Sciences, Shenzhen, China. [2]School of Airspace Science and Engineering, Shandong University, Weihai, China. [3]Weihai Research Institute of Industrial Technology of Shandong University, Weihai, China. [4]Department of Urology, Qilu Hospital, Cheeloo College of Medicine, Shandong University, Jinan, China. [5]Key Laboratory of Urinary Precision Diagnosis and Treatment in Universities of Shandong, Jinan, China. [6]School of Management Science and Engineering, Anhui University of Technology, Maanshan, China. [7]College of Mechanics and Engineering Science, Hohai University, Nanjing, China. [8]School of Mechanics and Construction Engineering, Jinan University, Guangzhou, China. [9]The Key Laboratory of Biomedical Imaging Science and System, Shenzhen Institutes of Advanced Technology, Chinese Academy of Sciences, Shenzhen, China. [10]Guangdong Provincial Key Laboratory of Multimodality Non-Invasive Brain-Computer Interfaces, Shenzhen Institutes of Advanced Technology, Chinese Academy of Sciences, Shenzhen, China. [11]Centre for Neurocognition and Social Behavior, Artificial Intelligence Research Institute, Shenzhen University of Advanced Technology, Shenzhen, China. [12]These authors contributed equally: Hanfei Li, Shuai Wang. [13]These authors jointly supervised this work: Kaikai Song, Yan Li, Zhiyuan Liu. ✉e-mail: songkaikai@sdu.edu.cn; yanli@sdu.edu.cn; zy.liu1@siat.ac.cn

remains challenging due to the bladder's soft and isotropic expansion. This necessitates the creation of a soft thin-film patch that can isotropically stretch and function under these conditions.

Addressing the bladder's isotropic deformation requires developing a soft, stretchable thin-film patch with reliable isotropic stretchability for precise signal acquisition and electrical stimulation. The key lies in stretchable conductive materials (SCM), where previous efforts have largely focused on uniaxial SCM, achieving over 200% stretchability, and in some cases, exceeding 500%[20–30], through techniques like spreading nanowires[26,31–36], using micro-crack gold films[22,37–39], or serpentine structures[22,40–43]. However, isotropic SCM studies are scarce, often employing a pre-stretch method[37,44–47] that introduces challenges due to mismatched Young's modulus, leading to pattern distortion and buckling. The isotropic stretchability, S_i, is defined as $(A_s/A_o - 1) \times 100\%$, where A_s is the area of the patch after isotropic stretch and A_o is its original area. An innovative approach by Sungryul Yun et al. bypassed these issues by embedding a melted silver nanowire network into a polymer, achieving ~68% isotropic stretchability without pre-stretching[36]. Given the bladder's capacity for 150% isotropic stretch when filled[14,48], developing a soft thin-film patch with sufficient isotropic stretchability is crucial for creating implantable BdMI systems.

Herein, we report a soft thin-film implantable BdMI capable of isotropic deformation and monitoring with electrical stimulation. The core of our BdMI is high-performance stretchable thin-film electrodes that remain conductive under isotropic strain. We developed a method involving thermal evaporation of gold on selected elastic polymeric substrates, resulting in a nano-needle structure within the polymer and a surficial conductive layer with a grooved structure. The thin film can achieve micrometer surface roughness, >800% isotropic stretchability, and 700% unidirectional stretchability, maintaining stable electrical performance over 50,000 cycles under 200% strain. We attribute this performance to localized thermal instability when hot gold clusters strike heat-sensitive soft polymer chains. Utilizing this film, we develop a multifunctional BdMI for neurogenic bladder management. In a rat model of SCI-induced bladder dysfunction, the implanted device successfully monitors bladder intravesical pressure, detects detrusor electromyographic activity, and provides electrical stimulation therapy. Therapeutic electrical stimulation over a period of 7 days significantly reduces involuntary bladder contraction frequency ($p < 0.05$) compared to SCI rats without implantation, validating the system's intervention capabilities. This work highlights potential for managing neurogenic bladder pathologies via real-time feedback and electrical stimulation, paving the way for personalized therapeutic strategies in chronic bladder disorders, thereby improving patient outcomes and quality of life.

Results and discussion

We designed a soft implantable bladder-machine interface (BdMI) for treating neurogenic bladder disease, which synchronizes with the host bladder's contractions while maintaining functional integrity (Fig. 1a). It offers real-time bladder intravesical pressure monitoring, electromyographic (EMG) recording of detrusor activity, and electrical stimulation intervention. Our fabrication method for isotropic stretchable electrodes allows precise patterning and large-scale production (Fig. S1). Scanning electron microscopy (SEM) shows a periodically grooved surface morphology (peak-to-valley distance = $2.5 \pm 1\,\mu m$), preserving the gold film's integrity during deformation (Fig. 1b–d), ensuring stable electrical performance. The resultant device (Fig. 1e) features its machinability and patterning performance. Post-implantation, two skull interfaces were established: a standard neural interface for electrical signals and stimulation, and a urodynamic interface for real-time bladder pressure monitoring (Fig. 1f). Performance tests show our electrode's uniaxial and isotropic stretchability exceeds 700% and 800%, respectively. Compared to other isotropic electrodes (Fig. 1g)[20,38,44–47,49–52], our electrode demonstrates superior capabilities.

To evaluate the electromechanical properties of our electrodes, we fabricated a 500 μm wide electrode (The electrodes used for animal experiments are made based on this electrode width), which showed excellent conductivity and adhesion even after 700% tensile deformation (Fig. 2a). During uniaxial stretching, the sheet resistance changed minimally under 100% strain, then gradually increased, with significant changes observed beyond 200% strain (Fig. 2b). Isotropic tensile testing showed sheet resistance changes of approximately 0.8×, 2.1×, and 24× at isotropic strains of 125, 300, and 525%, respectively (Fig. 2c). The resistance increased nearly 12 times at 300% isotropic strain (Fig. S2). Reducing electrode width to 200 μm, stability was maintained up to 200% strain, but resistance increased gradually beyond this, leading to failure at around 500% strain (Fig. S3a). Resistance remained stable under various tensile speeds, with a noted increase in hysteresis at higher speeds (Fig. S3b). Subjecting it to 50,000 cyclic tensile tests at 200% strain across frequencies from 0.05 to 2 Hz, the electrode displayed remarkable tensile cycling stability (Fig. 2d).

We also evaluated the cycling performance of the electrode under isotropic strain applied using a balloon expansion-based device, demonstrating good electrical performance and stability over 5000 cycles at about 250% isotropic strain (Fig. 2e, f, Video S1). Impedance tests post-fabrication and after 30 days showed preserved characteristics (Fig. S4). AC electrical stimulation tests confirmed electrode durability under stimulation parameters, with impedance decreasing rather than increasing, ensuring normal electrical performance under various current values from 5 to 50 mA (Fig. S5). These findings underscore the electrodes' robustness and reliability for long-term applications in dynamic strain environments.

Next, we delved into the underlying mechanism that endows the film with such exceptional isotropic stretchability. The morphology of the film was observed first. It showed the periodically grooved surface morphology (Fig. 3a, b, S6 and S7). Importantly, the grooved structure was fully expandable. As the isotropic strain applied increased to 800%, it was almost fully expanded with no significant cracks in the film, and the surface roughness of the film decreased (Fig. 3b and S8). Beyond 800%, larger cracks emerged, augmenting the roughness of the gold film (Fig. S8 and S9) and suggesting areas of gold film bulge from tearing. In comparison, the conventional microcracked stretchable gold film revealed many penetrating cracks, breaking the gold film into isolated "islands" and losing its electrical properties when suffering isotropic strain (Fig. S10). These findings demonstrate that BdMI's unique morphology confers excellent isotropic stretchability. It indicated that the expandable grooved surface structure of the conductive layer was the key to achieve such exceptional isotropic stretchability. Additionally, for uniaxial stretching of the gold film, it remained crack-free under 200% strain, explaining minimal resistance changes at this strain (Fig. 2a, S3a and S11). As strain increases beyond 200%, small cracks formed on the gold film surface to release stress, preserving the conductive pathway and overall conductivity of the electrode layer, until throughout cracks cut off the conductive pathway when uniaxial strain went up to 700% (Fig. S11 and S12).

To further understand the unique morphology of the electrode, the cross-section of the film was observed. It displayed periodic undulations, with an amplitude of $4 \pm 1\,\mu m$ and a wavelength of $3 \pm 2\,\mu m$ (Fig. 3c and S7). Notably, the amplitude of the grooved structure was much larger than that of conventional ones generated by pre-stretching the elastic substrate[29,30,44,47]. Additionally, we observed that the conductive layer of the film was composed of gold nanoneedles and elastic polymers (Fig. 3c right), indicating that evaporated gold nanoclusters gradually merged into the substrate during the deposition process, forming a conductive network within the composite layer. It was further deduced that this "merging" process of the

https://doi.org/10.1038/s41467-026-70680-0

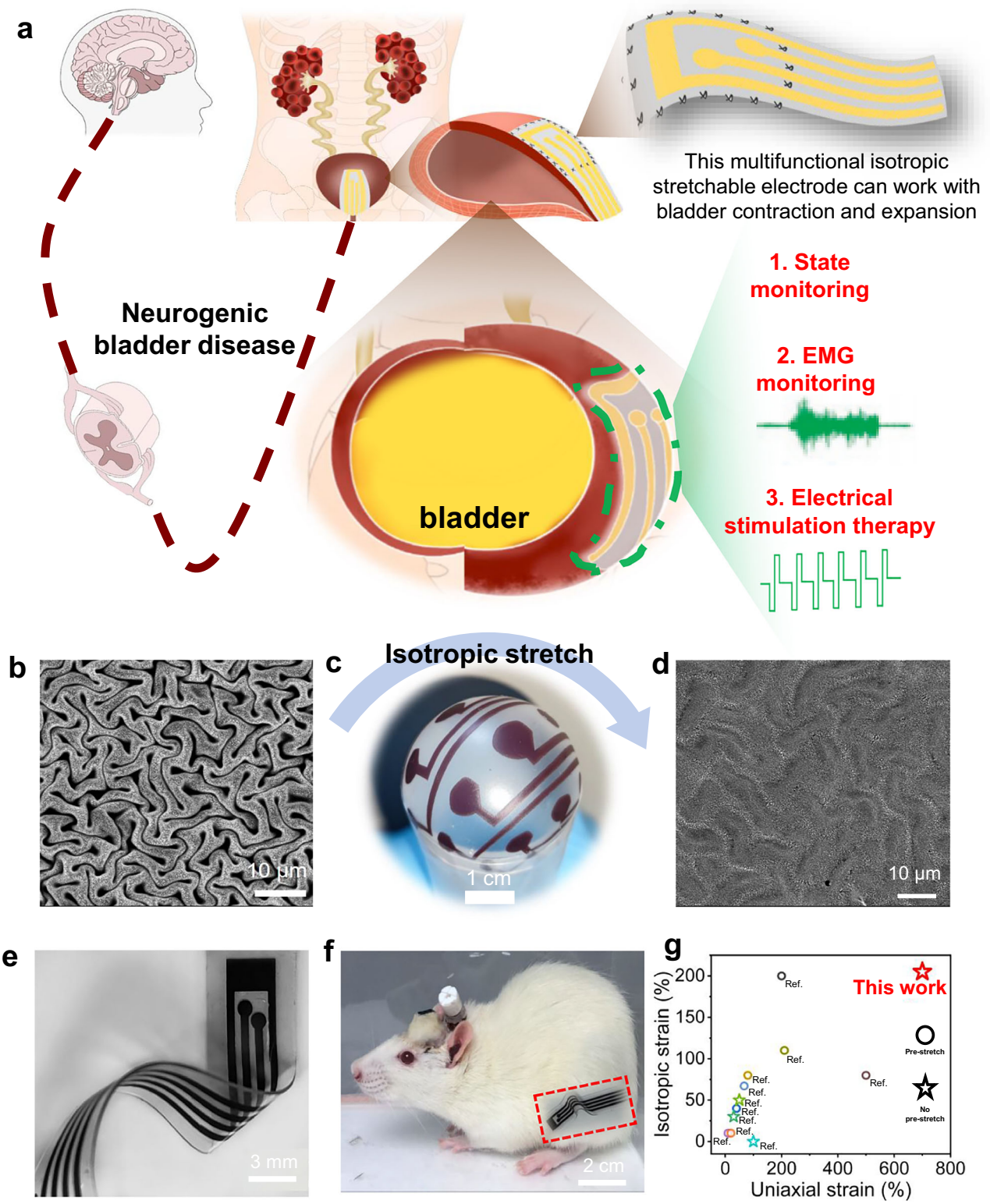

Fig. 1 | A bladder-machine interface (BdMI) utilizing intrinsically isotropic stretchable thin-film patches for the multimodal, chronically implantable treatment of neurogenic bladder dysfunction. a Schematic illustration of the BdMI system demonstrating its multifunctionality, including bladder state monitoring, electromyography (EMG) recording, and electrical stimulation therapy—highlighting its potential in treating neurogenic bladder disorders. **b** Scanning electron microscopy (SEM) image showing the microstructure of the intrinsic BdMI in the unstretched state. **c** Optical image of the BdMI undergoing isotropic stretching, demonstrating its mechanical compliance. **d** SEM image of the BdMI microstructure under isotropic stretching, confirming structural integrity. **e** Optical image of one sample of BdMI. **f** Photograph of a rat model with BdMI implanted. Implantation position is roughly marked in the red dashed rectangle. **g** Performance benchmarking of our high-performance stretchable electrode against reported isotropically stretchable electrodes, categorized into pre-stretched and non-pre-stretched types. Experiments were repeated independently (**b**, **d**) three times with similar results.

https://doi.org/10.1038/s41467-026-70680-0

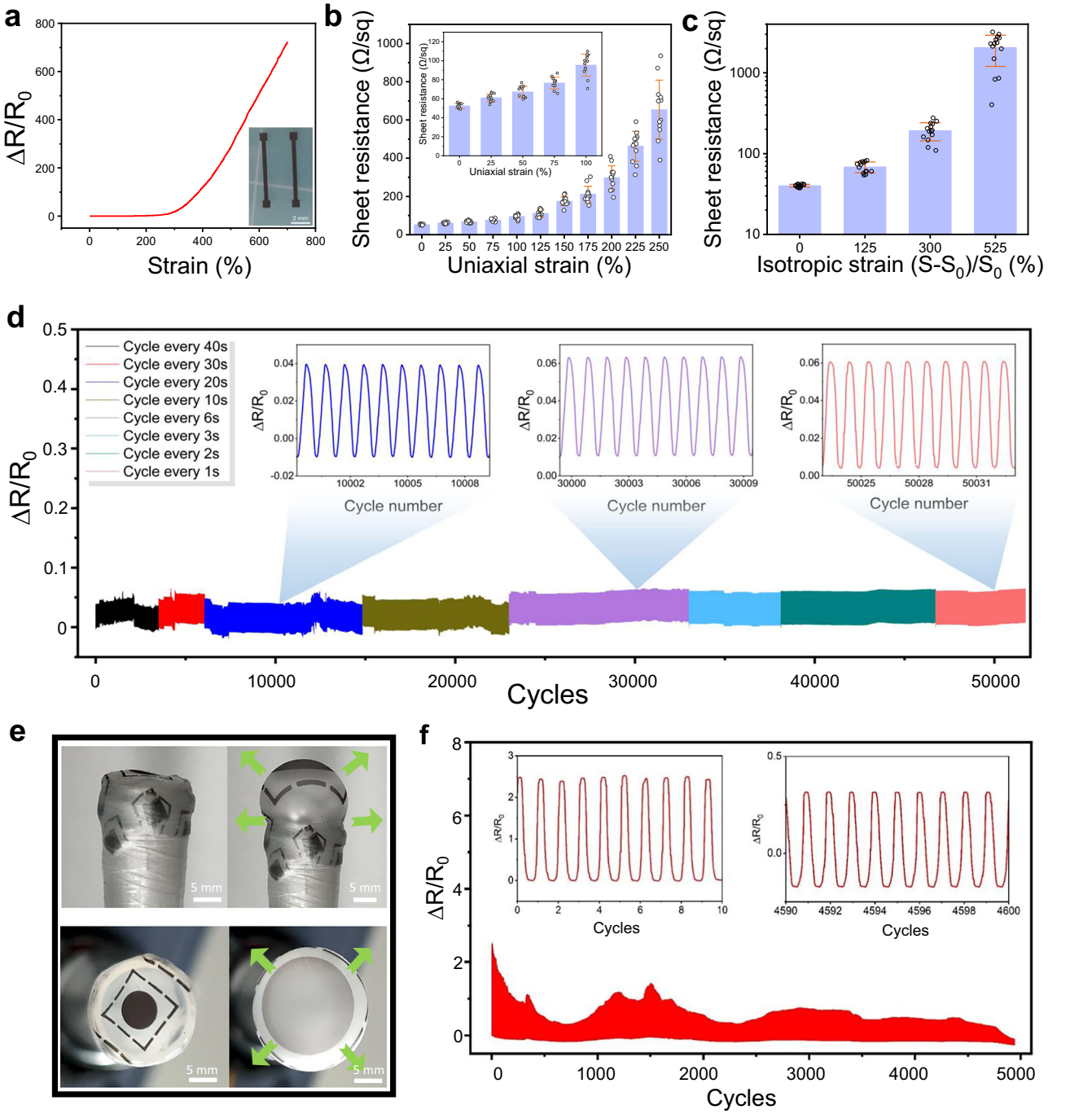

Fig. 2 | Performance characterization of the BdMI system. a Uniaxial stretchability testing of BdMI at a width of 500 μm. Stretchability of up to 700% is achieved. **b** Sheet resistance measurements of BdMI under unidirectional stretching ($n = 12$ independent experiments, data are presented as mean ± SD). **c** Sheet resistance measurements of BdMI during isotropic stretching ($n = 14$ independent experiments, data are presented as mean ± SD). **d** Cyclic stability testing of BdMI under 100% strain across varying stretching speeds, demonstrating stability over 50,000 cycles. **e** The testing setup of the isotropic stretchability of the BdMI. **f** Cyclic performance data of BdMI under isotropic stretching, highlighting durability and reliability over repeated cycles.

evaporated gold nanoclusters led to the buckling of the composite conductive layer. The driving force behind this could be the coupling effect of the localized heat from the hot evaporated gold nanoclusters and the migration of the soft polymer chains from the bottom to the surface. It could induce their localized convection effect in the surface of the film. This process effectively drew the soft polymer to the surface, inducing the unique morphology of the electrode. In order to investigate the bonding status between the gold film and the flexible substrate and verify whether the gold film is truly embedded in the polymer substrate, we deposited gold films of the same thickness on silicon wafers and ecoflex, and took SEM images and corresponding elemental analysis images for comparative analysis (Fig. S13). From the figure, it can be seen that after depositing a gold film of this thickness, the distribution of silicon elements in the underlying silicon chip is almost not displayed. The same conclusion can be drawn from the SEM and EDS images of the gold film edge, indicating that as long as this thickness of gold film can cover the substrate, the elements of the substrate cannot be measured. However, SEM and EDS images of gold films with the same thickness evaporated from the surface of ecoflex show that in addition to the distribution of gold elements, there are

https://doi.org/10.1038/s41467-026-70680-0

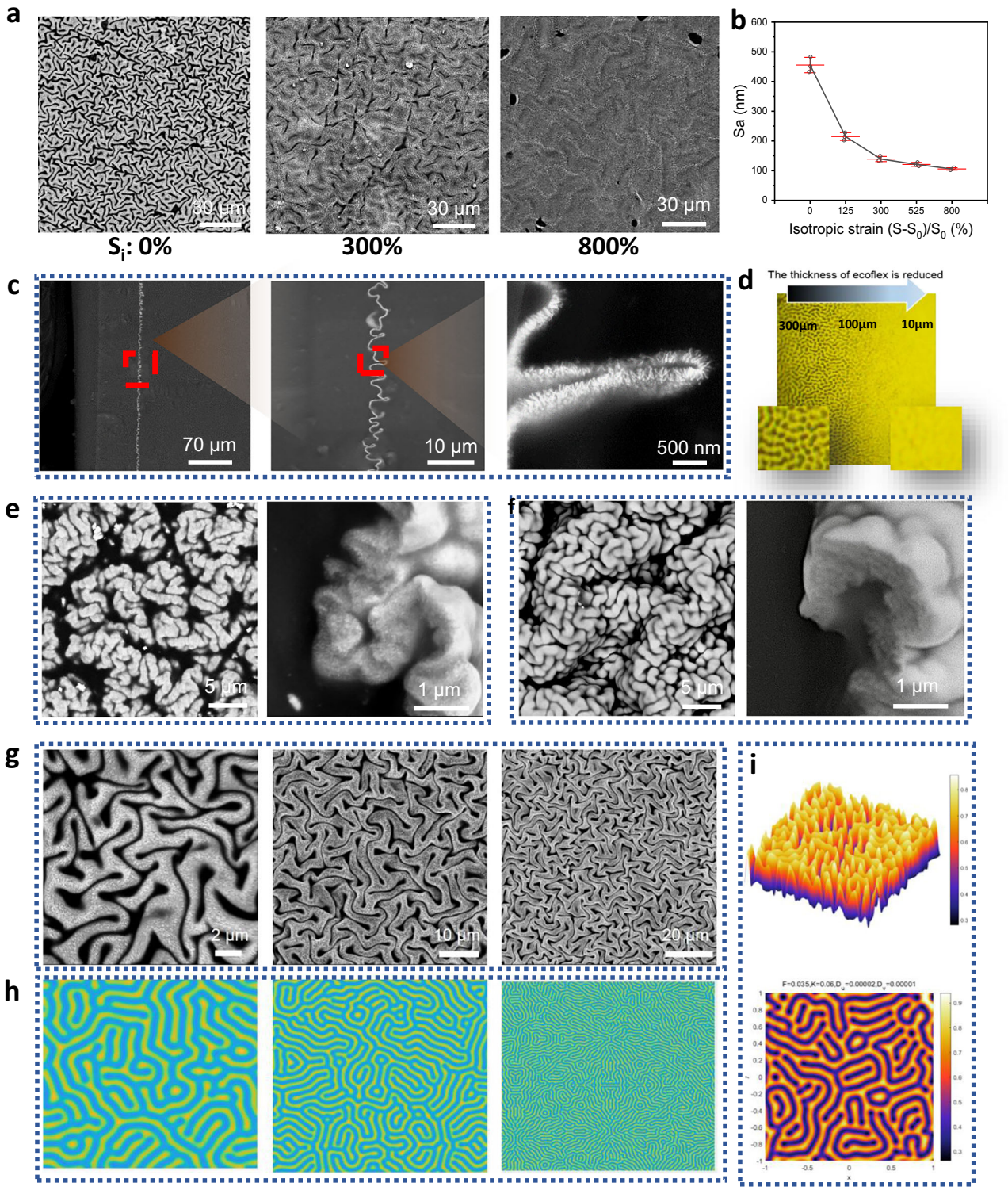

Fig. 3 | Investigation into the exceptional properties of BdMI. a SEM images of BdMI under isotropic stretching at 0%, 300%, and 800%. **b** Surface roughness of electrodes under varying isotropic strain ($n = 3$ independent experiments, data are presented as mean ± SD). **c** Cross-sectional view of the electrode after encapsulation. **d** Optical microscope image showcasing changes in gold film morphology as the thickness of the elastic substrate decreases from 300 to 10 μm. Front and cross-sectional SEM images of two isotropically stretchable electrodes based on Solaris substrate, with the following fabrication parameters: **e** gold film thickness of 400 nm, evaporation rate of 10 Å s^{-1}, and **f** gold film thickness of 1000 nm, evaporation rate of 50 Å s^{-1}. **g** SEM images of BdMI at various magnifications, in comparison of the typical Turing pattern (**h**). **i** 3D and front view of the Turing pattern simulated based on following parameters: F = 0.035, K = 0.06, Du = 0.00002, Dv = 0.00001 (see Text S1). Experiments were repeated independently (**a**, **c**, **e**–**h**) three times with similar results.

also many carbon, oxygen, and silicon elements (which are the main elements contained in the substrate), particularly evident at the bottom of the folds. This indicates that the evaporated gold film is embedded in the ecoflex flexible substrate.

To further understand the mechanism, we examined the impacts of substrate thickness (Fig. 3d) and the thickness of the evaporated gold film on the morphology (Fig. S14–S18). For the thin substrate (e.g., <100 μm), there would be no spontaneous grooved surface structure, opposite to that on thick substrate (e.g., 300 μm) (Fig. 3d). When the polymer was in small thickness, the convection migration of the soft polymer chain as discussed before would be weakened due to the confinement effect from the bottom of the film that was attached to a solid supporter. For the different thickness of the gold film, early-stage characterization showed spontaneous nanoscale buckling when 5 nm-thickness gold was deposited (Fig. S14), hinting at the convection happened at the very initial stage of the deposition of the gold film. Increasing the thickness of the gold film altered its surface morphology from smaller to larger folds with fewer but deeper folds (Fig. S15). This observation is corroborated by cross-sectional images of varying gold film thicknesses (Fig. S16–S18). Before reaching a certain thickness (~200 nm), the gold film lacks continuity, leading to subpar electrical performance and often non-conductivity. Comparative metallization studies (Fig. S19–S20) emphasized gold's unique interfacial behavior: Platinum and silver depositions under the same conditions resulted in traditional granular microstructures without spontaneous grooved structure. Additionally, leveraging our BdMI preparation experience, we used another commercialized silicone-based elastomer, Solaris, as the substrate and tested various preparation parameters (Fig. S21). With an evaporation rate of 50 Å s^{-1} and gold film thickness of 10000 Å, the electrode became conductive and achieve the uniaxial stretchability of 400% (Fig. S22). The electrode exhibited similar grooved structures (Fig. 3e, f and S23), further proving this method's generalizability.

To elucidate the detailed physical process behind this morphology, we proposed that the phenomenon could be explained by a typical Turing pattern process. Turing patterns, originally described by Alan Turing in his theory of morphogenesis, arise from the interaction between two or more chemical substances that diffuse at different rates. In the context of our electrode's morphology, the deposition of gold nanoclusters onto the soft polymer chains can be conceptualized as a diffusion process of gold within the substrate phase (Fig. 3g–i and S24)[53–56]. By applying the principles of Turing's two-phase diffusion, we gain insights into the final morphology of the gold film[55,57]. The mathematical details necessary for simulating the Turing pattern are provided in the Supporting Information Text S1. This theoretical framework helps to understand that how the distinct grooved structure in the electrode is not merely a result of mechanical deformations (Fig. S25) but are driven by underlying physical processes.

To assess the long-term monitoring and intervention capabilities of BdMI, we conducted implantation experiments using a healthy rat model (Fig. 4a, b). The active zone of BdMI, measuring 4.6 mm × 6 mm, consisted of a stretchable strain sensor module encapsulated by a protective layer and an electromyographic (EMG) acquisition and electrical stimulation module exposed for direct interaction (Fig. S26a). In-vitro experiments confirmed the durability of the stretchable strain sensor, which maintained stable performance after being stretched 1000 cycles at maximum strain of 50%, 100%, and 200% (Fig. S26b, c). According to Fig. S27a, the thickness of the device is about 300μm, and the strain coefficient of the strain sensor module is 0.14, 0.83, 6.01, 29.93, 57.27, 84.72, and 103.47 at 100, 200, 300, 400, 500, 600, and 700% deformation, respectively (Fig. S27b). It can be seen that the strain coefficient increases with the increase of deformation. This gives it the ability to monitor larger deformations. The strain sensor is a resistive strain sensing mechanism with a tensile hysteresis of 36–39%. Prior to in vivo experiments, the subcutaneous biocompatibility of Material 734—the soft–hard interface encapsulation of the BdMI—was assessed over 28 days. The material demonstrated histological scores and fibrous capsule thickness comparable to those of Ecoflex (Fig. S28). Upon suturing the active zone of BdMI onto the bladder surface (Fig. 4b), the bladder was gradually filled with physiological saline, inducing significant isotropic deformation of the BdMI as the bladder expanded (Fig. S29 and Video S2). Photographs document the uniform expansion of the bladder wall-sutured electrode upon bladder filling (Fig. S30). These results demonstrated that BdMI exhibited excellent conformality, with no tearing, detachment, or displacement during repeated isotropic stretching.

Two unencapsulated exposure points were designed for real-time bladder EMG signal monitoring and electrical stimulation, in combination with a reference electrode fixed at the rat's tail root. A fluid pathway connected to a pressure sensor via a Ruhr connector enabled traditional cystometry, while the electrical pathway linked the device to a digital multimeter, bioelectric acquisition system, and electrical stimulator via a skull connector (Fig. 4c). Dynamic datasets of intra-bladder pressure (IBP) (blue), mechanical strain (red), and bladder capacity (yellow) were recorded during multiple urine storage and voiding cycles in both acute (day 0, Fig. 4d) and chronic implantation models (day 10, Fig. 4e and Video S3). We compared BdMI resistance changes at different implantation sites in the rat bladder. BdMI at the trigone showed minimal deformation and a resistance change of 0.003. In contrast, implantation at the dome induced pronounced deformation with isotropic patterns and a larger resistance change of 0.06. This value approached the isotropic stretching range of BdMI (~0.5), indicating that the bladder model effectively represents the sensor's performance in highly deformable, isotropic environments (Fig. S31).

The resistance of the stretchable strain sensor increased gradually during urine storage and exhibited a sharp rise and recovery during micturition reflex, reflecting bladder contraction and emptying. Chronic implantation (day 10) demonstrated longer contraction intervals and lower IBP during urine storage compared to acute testing (day 0), indicating enhanced bladder compliance and good biocompatibility and stability of the stretchable strain sensor over time. Bladder stimulation experiments revealed that 25-s electrical stimulation epochs successfully induced bladder contractions, increasing pressure 4.2 mmHg (50 Hz, 500 μs pulse width, 3 mA) or 15.9 mmHg (50 Hz, 500 μs pulse width, 5 mA) from a baseline of 7–9 mmHg, whereas lower currents (1–2 mA) elicited negligible responses (<2 mmHg) (Fig. 4f, g and S32). While the induced pressure by 3 and 5 mA electrical stimulation epochs increases resembled those required for physiological urination, no urine expulsion occurred, likely due to uncoordinated bladder outlet opening (guarding reflex). Future studies could focus on simultaneously stimulating the bladder (micturition reflex) and relaxing the external urethral sphincter (augmenting reflex) to address detrusor-external sphincter dyssynergia and improve initial urethral flow[51,58,59]. Furthermore, fabricating multi-electrode arrays that cover a larger area of the detrusor muscle—rather than relying on single- or dual-point stimulation—may offer a promising solution. By activating multiple sites simultaneously or in programmed spatiotemporal sequences, coordinated contractions can be elicited across an extended region. This strategy aims to recruit a critical region of the bladder wall, generating sufficient synergistic force for effective voiding.

Additionally, BdMI accurately recorded bladder EMG signals near IBP peaks on both day 0 and day 28 (Fig. 4h–I and S33 and Video S4), demonstrating its capability to monitor multiple physiological signals for bladder analysis over extended implantation periods. These findings underscore the potential of BdMI for long-term bladder monitoring and regulation.

Building upon the promising in vivo results observed in healthy animal models—particularly in detecting bladder motor function and

https://doi.org/10.1038/s41467-026-70680-0

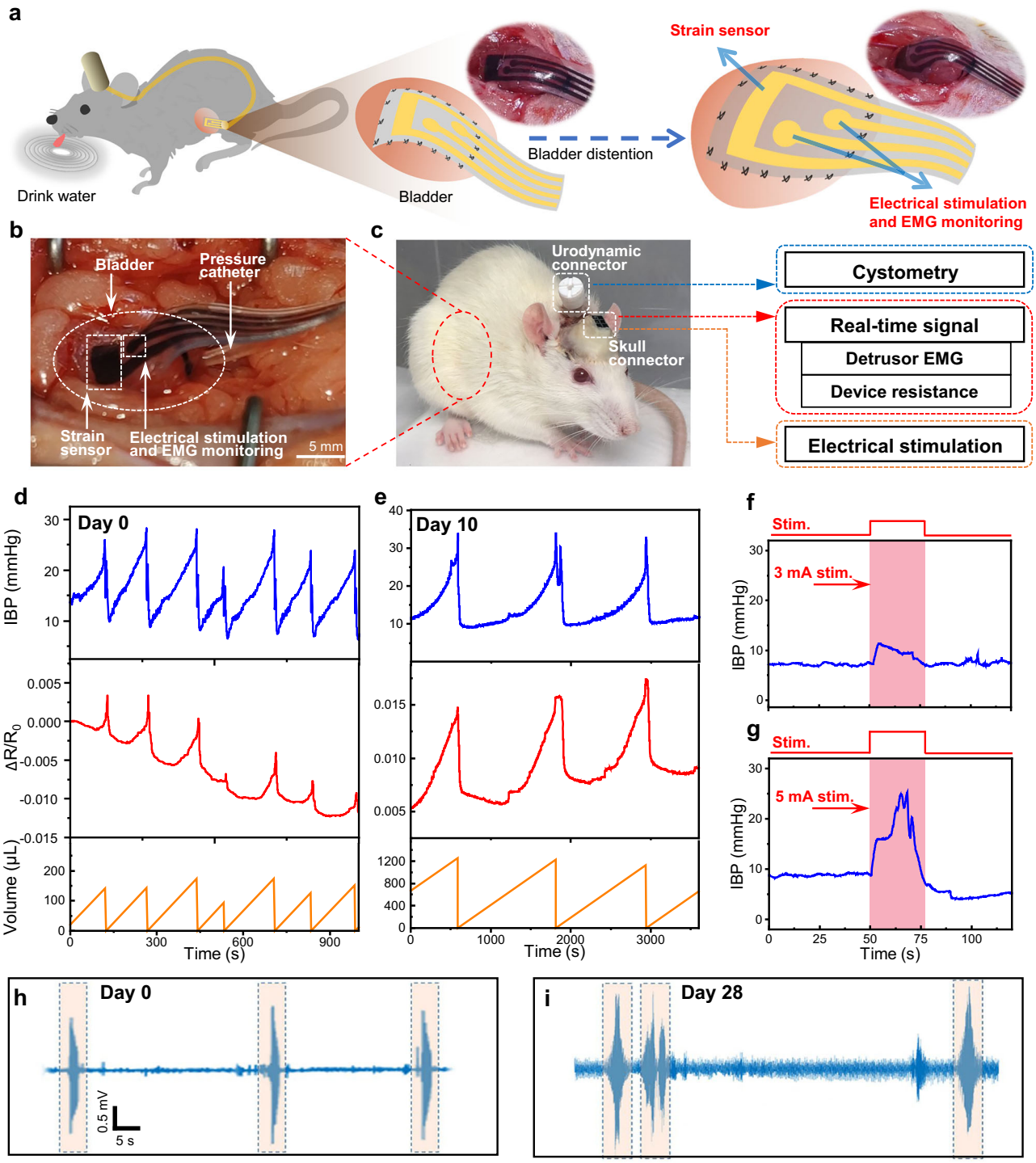

Fig. 4 | Long-term performance of BdMI implantation in the rat urinary system for real-time monitoring and intervention. a Schematic of the long-term experiment showing real-time bladder strain and EMG monitoring, combined with electrical stimulation in a rat model. **b** Photo of the rat urinary system implanted with BdMI, and **c** photo of the rat after BdMI implantation with head-mounted interface, where the implanted stretchable strain sensor, EMG monitoring channels, and stimulation channels were connected to a digital multimeter, bioelectrical recording system, and electrical stimulator, respectively, via cranial connectors. A pressure catheter was linked to a syringe pump and pressure sensor through a Ruhr connector for cystometric analysis. Continuous signal recordings on the day of implantation (**d**) and at day 10 post-implantation (**e**) show a consistent correlation among intravesical pressure (IBP), resistance changes of the electrode, and bladder filling. Bladder contractions and corresponding IBP increases elicited by electrical stimulation at 3 mA (**f**) and 5 mA (**g**) in acute settings. EMG signals recorded during urination events on the day of implantation (**h**) and at day 28 post-implantation (**i**). In (**f**, **g**), stim. indicates the electrical stimulation. Source data are provided as a Source data file.

delivering electrical stimulation—we further explored the potential of the BdMI for identifying and alleviating bladder overactivity. Previous studies had employed implantable bladder strain sensors in rodent models to monitor bladder overactivity or underactivity by detecting voiding contractions and evaluating contraction frequency[13–15]. These models typically induced acute bladder overactivity using agents such as acetic acid[14] or cyclophosphamide[13], resulting in shortened contraction intervals. However, such acute models, especially those

conducted under anesthesia, failed to recapitulate key clinical symptoms of overactive bladder, such as urinary urgency and detrusor overactivity (DO) during cystostomy evaluation.

To better simulate the clinical pathology of overactive bladder, we employed a spinal cord injury (SCI) rat model—a widely used and well-characterized model that exhibited increased detrusor overactivity due to neurogenic mechanisms[60]. All rats were randomly categorized into four groups: sham, SCI, SCI + sham electrical stimulation, and SCI + electrical stimulation. Rats underwent sham or SCI surgery on day 0, electrode implantation on day 21, cystostomy surgery on day 28, and urodynamic evaluation on day 29. We manually pressed the bladders daily, with electrical stimulation or sham stimulation starting on day 21 and lasting for 7 days (Fig. 5a). On day 8 post-electrode implantation, we concurrently monitored resistance change of the stretchable strain sensor and IBP to assess the ability of our stretchable strain sensors to distinguish between the physiological and pathological activities of the bladder via anesthesia urodynamic examination (Fig. 5b–f). We displayed a resistance curve of up to 3000 s (Fig. 5b), with a zoomed-in view of 800 s (Fig. 5c), and the corresponding IBP curve (Fig. 5d). Based on the urodynamic test results over five complete voiding cycles, we flagged three types of events: voiding contractions (urine excretion observed, marked with red triangles), non-voiding contractions (no urine excretion observed, and IBP amplitude >2.94 mmHg, marked by red hollow triangles), and non-clinically significant contractions (no urine excretion observed, and 1 mmHg <IBP amplitude <2.94 mmHg, marked by yellow hollow triangles). Close to the IBP peaks, the device resistance visually exhibited consistent signal trends (marked with dotted vertical lines, Fig. 5c, d). Specifically, as IBP peaks occurred during detrusor contraction and relaxation, the resistance detected by the stretchable strain sensor rose and recovered concurrently, resulting in an upward peak when the IBP peak appeared.

We further evaluated the potential of the BdMI to distinguish clinically significant bladder contractions—comprising voiding contractions and non-voiding contractions (NVCs)—from non-clinically significant contractions, as well as to differentiate between voiding contractions and NVCs. A representative set of resistance and IBP signals from one of five typical voiding cycles is shown in Fig. 5e, f. Given the apparent consistency in the peak amplitudes of both signals, we defined the amplitude of the normalized resistance curve (R/R_0) as the difference between its peak value and a predetermined threshold. This amplitude was then used as a quantitative parameter in our diagnostic model (Fig. 5e).

To evaluate the model's diagnostic performance, we employed receiver operating characteristic (ROC) curve analysis to assess the accuracy of R/R_0 amplitude in distinguishing clinically significant contractions from non-clinically significant ones (Fig. 5g). The area under the ROC curve (AUC) was 0.8699 (95% CI: 0.7702–0.9697, $P < 0.0001$), indicating strong diagnostic efficacy. The optimal cut-off value was determined to be 0.001075, yielding a specificity of 91.67% and a sensitivity of 72.97%. Following this, we applied the same approach to further evaluate the ability of the R/R_0 amplitude to distinguish between voiding contractions and NVCs (Fig. 5h). The AUC in this case was 0.7516 (95% CI: 0.5952–0.9079, $P = 0.0112$), suggesting moderate-to-high predictive accuracy. The optimal threshold was 0.001290, with specificity and sensitivity values of 85.71 and 56.52%, respectively. These results demonstrate the feasibility of using resistance amplitude detected by the stretchable strain sensor as a diagnostic biomarker to differentiate between various types of bladder contractions in vivo.

In neurogenic bladder rat models, our long-term implanted BdMI exhibited high diagnostic efficacy in distinguishing non-clinically significant contractions, non-voiding contractions, and voiding contractions, indicating that it can be reliably used for the diagnosis of physiological and pathological bladder function events, which has significant clinical implications. Based on this, the continuous diagnostic data from the BdMI motion sensor, designed to capture physiological and pathological contractile signals of bladder activity enable real-time feedback for initiating stimulation protocols (Fig. 5i). Specifically, the BdMI system monitors bladder strain after spinal cord injury and, using a validated cut-off value, differentiates in real time between physiological bladder status and pathological detrusor overactivity. Upon detection of detrusor overactivity, the BdMI stimulation protocol can be activated by clinicians to alleviate the condition.

To evaluate the therapeutic effect of localized bladder electrical stimulation by our BdMI on neurogenic bladder overactivity, the BdMI was implanted into rats, which subsequently received daily stimulation or sham stimulation for 1 week starting from day 21 post-SCI surgery (Fig. 5j). No significant differences were observed among the SCI, SCI + stimulation, and SCI + sham groups in terms of baseline pressure, maximum pressure, inter-contraction interval or body weight (Fig. 5k–n and S34b). However, key indicators such as, NVC frequency, bladder weight, and bladder-to-body weight ratio significantly increased, confirming the successful establishment of the neurogenic bladder overactivity model (Fig. 5k, o and S34a, c). Seven days post-implantation, the BdMI was observed to be encapsulated by omental tissue (Fig. S35), and post-implantation X-ray imaging of the BdMI device is shown in Fig. S36. Importantly, there were no observed differences in urodynamic parameters or histological outcomes—such as baseline pressure, maximum pressure, inter-contraction interval, bladder weight, body weight, or bladder histological analysis—between the SCI + stimulation and SCI + sham groups compared to the SCI group (Fig. 5k–n, S34 and S37). Urodynamic results supported a safe and therapeutic role of long-term electrical stimulation on bladder dysfunction. By comparing statistical data from different groups, it was found that the presence or absence of electrical stimulation had a significant impact on the frequency of NVCs in SCI rats, all other conditions being equal. The frequency of NVCs was higher in SCI and SCI + sham electrical stimulation rats compared to sham rats, while it decreased in SCI + electrical stimulation rats (Fig. 5o). The decrease in frequency suggests that BdMI can to some extent treat or alleviate NVCs caused by SCI, restoring NVCs frequency to levels close to those without SCI (Fig. 5o). Further analysis of NVC amplitude, integrated with the data from Fig. 5o, demonstrated that electrical stimulation mitigated the frequency of NVCs in SCI rats without affecting their amplitude (Fig. S38). Potential mechanisms of bladder electrical stimulation may include promoting neovascularization in the submucosal layer, inhibiting afferent C fiber activity, and affecting other lower urinary tract reflex mechanisms in the spinal reflex pathway[19,61].

Future research should focus on identifying optimal electrical stimulation parameters and investigating associated mechanisms. The experiments conducted thus far have demonstrated the safety and effectiveness of our BdMI system in orchestrating the diagnosis and treatment processes for neurogenic diseases. Compared with several other similar works (Table S1)[48,62,63], BdMI has better adaptive modulus, superior isotropic stretchability, rich and stable functional integration, and simpler preparation process. In Video S5, it can be seen that after 3 months of implantation of BdMI, the rat can still move freely and healthily, which also reflects the stability, adaptability, and good biocompatibility of BdMI. At the same time, we conducted aging tests on BdMI. We placed the prepared BdMI in PBS buffer solution to simulate the in vivo environment and placed it in a 60 °C oven for 4 weeks. According to the principle of time temperature equivalence, this environment is equivalent to being placed within the body temperature range for 2–3 months and at room temperature for 6–8 months. According to Fig. S39, it can be seen that there is no significant change in the surface morphology of the electrode before and after the aging test (Fig. S39a). The impedance change of the two groups of electrodes before and after the aging test was less than 5% (Fig. S39b), and the tensile conductivity decreased by about 10–15% (Fig. S39c). These data

https://doi.org/10.1038/s41467-026-70680-0

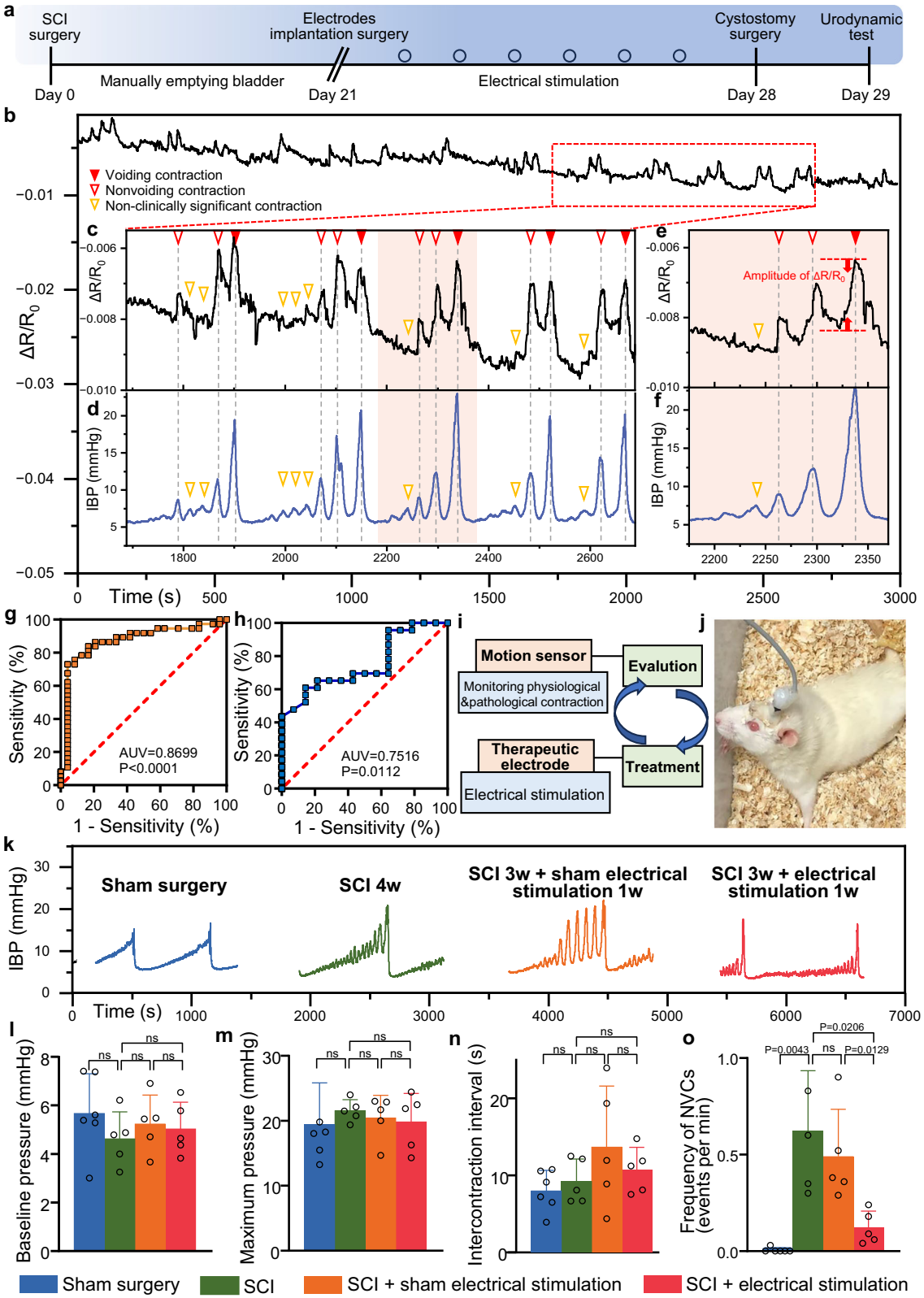

confirm that our device performance is relatively stable and can meet most usage scenarios. The damage caused to rats during the device implantation process, and the prolonged placement of the device in the body, are acceptable for rats. Finally, it is our hope to eventually replace bladder pressure monitoring with deformation sensors for disease diagnosis and subsequent electrical stimulation intervention, thereby achieving disease diagnosis, monitoring, and intervention. This approach could revolutionize the way we manage and treat bladder dysfunctions, providing a more integrated and patient-friendly solution.

In conclusion, this research introduced a novel thin-film implantable bladder-machine interface (BdMI) with the capacity of isotropic deformation monitoring and electrical stimulation. The core of our BdMI is high-performance stretchable thin-film electrodes that retain

Fig. 5 | Assessment and modulation of neurogenic bladder dysfunction following spinal cord injury (SCI). a Schematic of the experimental timeline. Rats underwent sham or SCI surgery on day 0, electrode implantation on day 21, cystostomy on day 28, and urodynamic testing on day 29. Electrical stimulation or sham treatment was applied from days 21 to 28. **b** Resistance change of the stretchable strain sensor over a 3000-s period. Representative traces showing resistance change (**c**) and intra-bladder pressure (**d**), illustrating voiding contractions (VC), non-voiding contractions (NVC), and non-clinically significant contractions (NCSC). **e**, **f** Close-up views of sensor resistance and IBP during a complete voiding cycle, with $\Delta R/R_0$ used to quantify contraction amplitude. **g**, **h** ROC curves evaluating $\Delta R/R_0$ for distinguishing NCSC and NVC events. **i** Workflow summarizing electrical stimulation therapy and bladder function evaluation via implantable electrodes. **j** Image of a freely moving paraplegic rat receiving bladder stimulation via a skull-mounted interface. **k** Representative IBP traces and group comparisons of **l** baseline pressure, **m** peak pressure, **n** inter-contraction interval, and **o** NVC frequency across the sham group ($n = 6$ biologically independent experiments), SCI group ($n = 5$ biologically independent experiments), SCI + sham stimulation group ($n = 5$ biologically independent experiments), and SCI + stimulation group ($n = 5$ biologically independent experiments). Data is presented as mean ± SD. Statistical analysis (in **g**, **h**) used the one-sided Mann–Whitney tests. Statistical analysis (in **i**–**o**) used the two-sided unpaired t-tests, Welch's t-tests, or Mann–Whitney tests, as appropriate (see Table S2 for details). ns not significant. Source data are provided as a Source data file.

conductivity under isotropic strain, achieved through a method of thermal evaporation of gold on selected elastic polymeric substrates. The resulting thin film demonstrated exceptional durability and stretchability, maintaining stable electrical performance over 50,000 cycles under 200% strain. The application of this film in a multifunctional BdMI for neurogenic bladder management was validated in a rat model of SCI-induced bladder dysfunction. The implanted device successfully monitored bladder intravesical pressure, detected detrusor electromyographic activity, and provided electrical stimulation therapy over a period of 7 days without adverse effects. Notably, therapeutic electrical stimulation significantly reduced the frequency of involuntary bladder contractions, thus confirming the system's therapeutic capabilities. This research underscores the potential of such an interface for managing neurogenic bladder pathologies through real-time feedback and electrical stimulation. The development of this BdMI paves the way for more personalized therapeutic strategies in the treatment of chronic bladder disorders. It offers a promising avenue for improving patient outcomes and quality of life, and warrants further investigation and development for clinical application. Future studies should focus on long-term effects of the device, as well as potential improvements to enhance its performance and applicability. Besides, identifying optimal electrical stimulation parameters and investigating associated mechanisms should be conducted in the future.

Methods

Materials

Ecoflex 00-20 was obtained from Smooth-On. Flexible printed circuit boards (FPCB) were designed and manufactured by Huasheng Precision Metal Company (Shenzhen, China). Anisotropic conductive adhesive (3M9703) was purchased from Minnesota Mining & Manufacturing Company. A stainless steel mask was purchased from Xingjixin Electronic Materials Corporation (Shenzhen, China). Copper wire (20 μm in diameter) and all other common reagents were supplied by Sinopharm Chemical Reagent Co., Ltd.

Preparation of the BdMI

The A and B components of Ecoflex 00-20 were mixed at a 1:1 mass ratio using a Thinky mixer for defoaming. The mixture was then spin-coated at 250 rpm using a homogenizer to prepare Ecoflex substrates with a thickness of 200–300 μm. Finally, the films were cured in an oven at 60 °C for 3 min. The desired electrode pattern was first marked on a PET film using a marking machine. The PET mask was then aligned and attached to the Ecoflex substrate. The masked substrate was loaded into a thermal evaporation system, where a 400 nm gold layer was deposited at a rate of 10 Å s^{-1} with a source-to-substrate distance of 60 cm. Following deposition, the sample was annealed at 60 °C for 48 h to enhance gold-electrode adhesion. Then, the sensing points and soft–hard interface regions requiring exposure were masked with high-temperature tape (The high-temperature tape is a PI tape, which is used to shield the electrode pattern of the sensing point and the soft–hard interface, protecting these areas from infiltration before the packaging layer is completely cured. The specific packaging effect can refer to Fig. S40). The electrode was then placed on a spin coater, and the uniformly mixed Ecoflex 00-20 (prepared in Step 1) was dispensed onto the surface. Spin coating was performed at 2000 rpm to achieve uniform Ecoflex distribution. After spin coating, the high-temperature tape was carefully removed using tweezers. Finally, the electrode was thermally cured at 120 °C for 12 h to complete the encapsulation process.

Soft and hard interface connection

The soft–hard interface connection was established by aligning the PCB board with the gold finger contacts of the electrode. The assembly was then tightly wrapped with a sealing film (minimum 10 layers) to create physical compression between the PCB and electrode contacts. This configuration ensured both electrical conductivity and mechanical stability by minimizing soft–hard component displacement. Finally, a 734 adhesive layer was applied to the exterior and cured, providing complete interface encapsulation for optimal stability and hermetic sealing.

Ethic statement

Wild-type Sprague Dawley 8-week-old female rats (200–300 g, Beijing Vital River) were housed in pairs under specific pathogen-free (SPF) conditions, with ambient temperature maintained at 22 ± 1 °C and relative humidity at 50 ± 10%. The animals were provided with unrestricted access to food and water while maintained under a 12 h:12 h light:dark cycle. All treatment procedures and animal welfare considerations adhered strictly to national regulations pertaining to animal experimentation. The Laboratory Animal Ethical and Welfare Committee of Shandong University Cheeloo College of Medicine reviewed and sanctioned all animal protocols (Approval No. 21128), which also aligned with the guidelines of the Care and Use of Laboratory Animals by the National Institutes of Health, Bethesda, MD, USA.

Anesthetized cystometry

Cystometry was conducted under urethane anesthesia (1.2 g/kg, Sigma). The bladder dome was exposed through a midline incision, followed by the insertion of a PE50 tube secured with a purse-string suture. The tube was then connected to a Genie-Touch syringe pump (Kent Scientific) and a pressure transducer (ADInstruments) through a T-junction. Room-temperature saline was gradually introduced into the bladder at 0.06 mL/min, and IBP was recorded via the PowerLab system (ADInstruments). NVCs characterized by spontaneous detrusor contractions without voiding and an amplitude of up to 2.94 mmHg (4 cmH_2O) were analyzed as per existing literature[64,65], Once a stable pattern was established, data from each animal were collated and analyzed using Origin (OriginLab) software to derive parameters such as maximum pressure, baseline pressure, and inter-contraction interval. The frequency of NVCs was also studied. The capacity of our strain sensors to differentiate between voiding and non-

voiding contractions across all types of contraction waveforms was assessed. For this, IBP waves featuring IBP amplitudes less than 2.94 mmHg but exceeding 1 mmHg were defined as non-clinically significant contractions.

Implantation of BdMI

In the aforementioned anesthetic urodynamic steps, following the secure placement of the PE50 catheter, an electrode was affixed to the bladder wall under microscopic guidance using an 8-0 suture. The stretchable strain sensor was interfaced with a digital multimeter device (NDM2041, OWON), and data were recorded using NDM PC software (OWON), utilizing a custom-developed script for resistance variation measurements. The electrode channels for EMG monitoring and electrical stimulation were connected to multi-channel bioelectric acquisition device and a commercial neurostimulator (Pins Medical), separately.

Preparation of SCI rat model implanted with BdMI

Under isoflurane anesthesia, the rats' dorsal region was sterilized. An incision was made at the T10 location on the back of the rats. The T10 (8th thoracic vertebra) segment spine was exposed, and the T8–T10 segments on either side were separated. The spinal cord was transected at T10, and a sterile sponge was positioned between the severed spinal cord ends. The sham-operated group of rats underwent an identical procedure except for the T10 spinal cord transection and served as controls. Manual bladder expression continued until spontaneous voiding resumed. On day 21 post-SCI, bladder electrodes and skull junctions were implanted, PE50 catheters and Ruhr junctions on day 28, followed by anesthetic cytometry on day 30. To ensure empty bladders, they were manually expressed prior to electrical stimulation. The electrical stimulation was administered in a week through skull junctions using a commercial neurostimulator (Pins Medical), which emitted square waves of 0.2 ms duration, frequencies of 20 Hz, and a duration of 60 min. The current intensity was calibrated to the maximum tolerable level within a range of 0.5–2 mA. Rats in the sham-electrical stimulation group underwent the same procedure without electrical stimulation and were compared as controls.

Biocompatibility testing

Rats were humanely euthanized, and their circulatory systems were perfused with 4% paraformaldehyde (PFA, Servicebio) for fixation. Whole bladders or the skin with material implanted in the subcutaneous area were then isolated, post-fixed overnight in 4% PFA, and subsequently embedded in paraffin. Tissue sections were stained with hematoxylin and eosin (H&E) or Masson's trichrome staining kit (Solarbio) according to standard protocols. The area of bladder fibrosis was quantified using ImageJ software. The severity of bladder inflammation was assessed using a previously reported scoring system[66]. The histological evaluation of skin tissue was performed according to the ISO 10993-6:2016 guidelines.

Statistical analysis

Data were collected in an unbiased manner, with the experimenter blinded to treatment groups during the final analysis. Results are presented as mean ± standard deviation (SD). Depending on data distribution and variance, appropriate statistical tests—including two-tailed unpaired t-tests, Welch's t-tests, or Mann–Whitney U tests, One-way ANOVA, or Welch's ANOVA test—were applied. Statistical significance was defined as $p < 0.05$. Receiver operating characteristic (ROC) curve analysis was conducted to evaluate the diagnostic performance of the R/R_0 wave amplitude in distinguishing voiding contractions, non-voiding contractions, and non-clinically significant contractions. Detailed statistical outcomes are provided in Table S2.

Reporting summary

Further information on research design is available in the Nature Portfolio Reporting Summary linked to this article.

Data availability

All data supporting the findings of this study are available within the article and its supplementary files. Any additional requests for information can be directed to, and will be fulfilled by, the corresponding authors. Source data are provided with this paper.

References

1. Haylen, B. T. et al. An International Urogynecological Association (IUGA)/International Continence Society (ICS) joint report on the terminology for female pelvic organ prolapse (POP). *Int. Urogynecology J.* **27**, 165–194 (2016).
2. Safiri, S., Kolahi, A.-A., Naghavi, M. & Global Burden of Disease Bladder Cancer Collaborators. Global, regional and national burden of bladder cancer and its attributable risk factors in 204 countries and territories, 1990–2019: a systematic analysis for the Global Burden of Disease study 2019. *BMJ Glob. Health* **6**, e004128 (2021).
3. Irwin, D. E., Kopp, Z. S., Agatep, B., Milsom, I. & Abrams, P. Worldwide prevalence estimates of lower urinary tract symptoms, overactive bladder, urinary incontinence and bladder outlet obstruction. *BJU Int.* **108**, 1132–1138 (2011).
4. Quadri, S. A. et al. Recent update on basic mechanisms of spinal cord injury. *Neurosurg. Rev.* **43**, 425–441 (2018).
5. Anjum, A. et al. Spinal cord injury: pathophysiology, multimolecular interactions, and underlying recovery mechanisms. *Int. J. Mol. Sci.* **21**, 7533 (2020).
6. Lv, L., Li, W., Guo, D., Shi, B. & Li, Y. Early sacral neuromodulation prevented detrusor overactivity in rats with spinal cord injury. *Neuromodulation Technol Neural Interface* **28**, 746–756 (2025).
7. Panicker, J. N. Neurogenic bladder: epidemiology, diagnosis, and management. *Semin. Neurol.* **40**, 569–579 (2020).
8. Groen, J. et al. Summary of European Association of Urology (EAU) Guidelines on Neuro-Urology. *Eur. Urol.* **69**, 324–333 (2016).
9. Ersoz, M. & Akyuz, M. Bladder-filling sensation in patients with spinal cord injury and the potential for sensation-dependent bladder emptying. *Spinal Cord.* **42**, 110–116 (2004).
10. de Sèze, M., Ruffion, A., Denys, P., Joseph, P.-A. & Perrouin-Verbe, B. The neurogenic bladder in multiple sclerosis: review of the literature and proposal of management guidelines. *Mult. Scler. J.* **13**, 915–928 (2007).
11. Ross Lawrenson, J.-J. W., Vlachonikolis, I., Farmer, C. & Glickman, S. Renal failure in patients with neurogenic lower urinary tract dysfunction. *Neuroepidemiology* **20**, 138–143 (2001).
12. Wyndaele, J.-J. The management of neurogenic lower urinary tract dysfunction after spinal cord injury. *Nat. Rev. Urol.* **13**, 705–714 (2016).
13. Mickle, A. D. et al. A wireless closed-loop system for optogenetic peripheral neuromodulation. *Nature* **565**, 361–365 (2019).
14. Oh, B. et al. Ultra-soft and highly stretchable tissue-adhesive hydrogel based multifunctional implantable sensor for monitoring of overactive bladder. *Biosens. Bioelectron.* **225**, 115060 (2023).
15. Jang, T.-M. et al. Expandable and implantable bioelectronic complex for analyzing and regulating real-time activity of the urinary bladder. *Sci. Adv.* **6**, eabc9675 (2020).
16. Yan, D. et al. Ultracompliant carbon nanotube direct bladder device. *Adv. Healthc. Mater.* **8**, e1900477 (2019).
17. Majerus, S. J. A. et al. Feasibility of real-time conditional sacral neuromodulation using wireless bladder pressure sensor. *IEEE Trans. Neural Syst. Rehabil. Eng.* **29**, 2067–2075 (2021).
18. Ouyang, Z., Sperry, Z. J., Barrera, N. D. & Bruns, T. M. Real-time bladder pressure estimation for closed-loop control in a detrusor

overactivity model. *IEEE Trans. Neural Syst. Rehabil. Eng.* **27**, 1209–1216 (2019).
19. Hong, C. H. et al. The effect of intravesical electrical stimulation on bladder function and synaptic neurotransmission in the rat spinal cord after spinal cord injury. *BJU Int.* **103**, 1136–1141 (2009).
20. Hong, J.-Y., Kim, W., Choi, D., Kong, J. & Park, H. S. Omnidirectionally stretchable and transparent graphene electrodes. *ACS Nano* **10**, 9446–9455 (2016).
21. Liu, J. et al. Intrinsically stretchable electrode array enabled in vivo electrophysiological mapping of atrial fibrillation at cellular resolution. *Proc. Natl. Acad. Sci. USA* **117**, 14769–14778 (2020).
22. Huang, S., Liu, Y., Zhao, Y., Ren, Z. & Guo, C. F. Flexible electronics: stretchable electrodes and their future. *Adv. Funct. Mater.* **29**, 1805924 (2018).
23. Yi, J. et al. Water-responsive supercontractile polymer films for bioelectronic interfaces. *Nature* **624**, 295–302 (2023).
24. Jiang, Y. et al. Topological supramolecular network enabled high-conductivity, stretchable organic bioelectronics. *Science* **375**, 1411–1417 (2022).
25. Xiang, Z. et al. Progress of flexible electronics in neural interfacing—a self-adaptive non-invasive neural ribbon electrode for small nerves recording. *Adv. Mater.* **28**, 4472–4479 (2015).
26. Miyamoto, A. et al. Inflammation-free, gas-permeable, lightweight, stretchable on-skin electronics with nanomeshes. *Nat. Nanotechnol.* **12**, 907–913 (2017).
27. Yu, M. et al. Self-closing stretchable cuff electrodes for peripheral nerve stimulation and electromyographic signal recording. *ACS Appl. Mater. Interfaces* **15**, 7663–7672 (2023).
28. Lee, S. et al. Toward bioelectronic medicine—neuromodulation of small peripheral nerves using flexible neural clip. *Adv. Sci.* **4**, 1700149 (2017).
29. Li, H. et al. Flexible and stretchable implantable devices for peripheral neuromuscular electrophysiology. *Nanoscale* **16**, 6402–6428 (2024).
30. Han, F. et al. Hybrid microstructure-based stretchable biosensors for multi-physiological signal sensing. *eScience* **5**, 100327 (2025).
31. Tybrandt, K. et al. High-density stretchable electrode grids for chronic neural recording. *Adv. Mater.* **30**, 1706520 (2018).
32. Choi, S. et al. Highly conductive, stretchable and biocompatible Ag–Au core–sheath nanowire composite for wearable and implantable bioelectronics. *Nat. Nanotechnol.* **13**, 1048–1056 (2018).
33. An, B. W., Heo, S., Ji, S., Bien, F. & Park, J.-U. Transparent and flexible fingerprint sensor array with multiplexed detection of tactile pressure and skin temperature. *Nat. Commun.* **9**, 2458 (2018).
34. Qi, D. et al. Highly stretchable, compliant, polymeric microelectrode arrays for in vivo electrophysiological interfacing. *Adv. Mater.* **29**, 1702800 (2017).
35. Amjadi, M., Yoon, Y. J. & Park, I. Ultra-stretchable and skin-mountable strain sensors using carbon nanotubes–Ecoflex nanocomposites. *Nanotechnology* **26**, 375501 (2015).
36. Yun, S. et al. Compliant silver nanowire-polymer composite electrodes for bistable large strain actuation. *Adv. Mater.* **24**, 1321–1327 (2012).
37. Li, H. et al. A hybrid strategy-based ultra-narrow stretchable microelectrodes with cell-level resolution. *Adv. Funct. Mater.* **33**, 2300859 (2023).
38. Kim, S. W., Lee, S., Kim, D., Lee, S. G. & Cho, K. Omnidirectionally stretchable metal films with preformed radial nanocracks for soft electronics. *ACS Appl. Nano Mater.* **3**, 7192–7200 (2020).
39. Matsuhisa, N. et al. High-transconductance stretchable transistors achieved by controlled gold microcrack morphology. *Adv. Electron. Mater.* **5**, 1900347 (2019).
40. Zhou, C. et al. Stretchable electrical cell-substrate impedance sensor platform for monitoring cell monolayers under strain. *Sens. Actuators B Chem.* **336**, 129656 (2021).
41. Ji, B. et al. Flexible and stretchable opto-electric neural interface for low-noise electrocorticogram recordings and neuromodulation in vivo. *Biosens. Bioelectron.* **153**, 112009 (2020).
42. Didier, C., Kundu, A. & Rajaraman, S. Capabilities and limitations of 3D printed microserpentines and integrated 3D electrodes for stretchable and conformable biosensor applications. *Microsyst. Nanoeng.* **6**, 15 (2020).
43. Choi, Y. S. et al. Stretchable, dynamic covalent polymers for soft, long-lived bioresorbable electronic stimulators designed to facilitate neuromuscular regeneration. *Nat. Commun.* **11**, 5990 (2020).
44. Lee, G. et al. Omnidirectionally and highly stretchable conductive electrodes based on noncoplanar zigzag mesh silver nanowire arrays. *Adv. Electron. Mater.* **2**, 1600158 (2016).
45. Yu, J. et al. Omnidirectionally stretchable high-performance supercapacitor based on isotropic buckled carbon nanotube films. *ACS Nano* **10**, 5204–5211 (2016).
46. Nam, I. et al. Omnidirectionally stretchable, high performance supercapacitors based on a graphene–carbon-nanotube layered structure. *Nano Energy* **15**, 33–42 (2015).
47. Görrn, P., Cao, W. & Wagner, S. Isotropically stretchable gold conductors on elastomeric substrates. *Soft Matter* **7**, 7177–7180 (2011).
48. Lee, J. H. et al. Wireless, fully implantable and expandable electronic system for bidirectional electrical neuromodulation of the urinary bladder. *ACS Nano* **17**, 8511–8520 (2023).
49. Ding, C. et al. Omnidirectionally stretchable electrodes based on wrinkled silver nanowires through the shrinkage of electrospun polymer fibers. *J. Mater. Chem. C* **8**, 16798–16807 (2020).
50. Kim, B. S. et al. Biaxial stretchability and transparency of Ag nanowire 2D mass-spring networks prepared by floating compression. *ACS Appl. Mater. Interfaces* **9**, 10865–10873 (2017).
51. Kim, B. S. et al. 2D reentrant auxetic structures of graphene/CNT networks for omnidirectionally stretchable supercapacitors. *Nanoscale* **9**, 13272–13280 (2017).
52. Roh, E., Lee, H. B., Kim, D. I. & Lee, N. E. A solution-processable, omnidirectionally stretchable, and high-pressure-sensitive piezoresistive device. *Adv. Mater.* **29**, 1703004 (2017).
53. Schwartzkopf, M. et al. Real-time monitoring of morphology and optical properties during sputter deposition for tailoring metal–polymer interfaces. *ACS Appl. Mater. Interfaces* **7**, 13547–13556 (2015).
54. Zaporojtchenko, V. et al. Formation of metal–polymer interfaces by metal evaporation: influence of deposition parameters and defects. *Microelectron. Eng.* **50**, 465–471 (2000).
55. Bánsági, T., Vanag, V. K. & Epstein, I. R. Tomography of reaction-diffusion microemulsions reveals three-dimensional turing patterns. *Science* **331**, 1309–1312 (2011).
56. Ramesh, G. V., Porel, S. & Radhakrishnan, T. P. Polymer thin films embedded with in situ grown metal nanoparticles. *Chem. Soc. Rev.* **38**, 2646 (2009).
57. Shoji, H., Yamada, K., Ueyama, D. & Ohta, T. Turing patterns in three dimensions. *Phys. Rev. E* **75**, 046212 (2007).
58. Danziger, Z. C. & Grill, W. M. Sensory feedback from the urethra evokes state-dependent lower urinary tract reflexes in rat. *J. Physiol.* **595**, 5687–5698 (2017).
59. Kavanagh, A. et al. Surveillance urodynamics for neurogenic lower urinary tract dysfunction: a systematic review. *Can. Urol. Assoc. J.* **13**, 133 (2018).
60. Ferreira, A., Nascimento, D. & Cruz, C. D. Molecular mechanism operating in animal models of neurogenic detrusor overactivity: a systematic review focusing on bladder dysfunction of neurogenic origin. *Int. J. Mol. Sci.* **24**, 3273 (2023).
61. Cao, T. et al. Low-frequency intravesical electrical stimulation for the treatment of acute urinary retention: a promising therapeutic approach. *Front. Med.* **8**, 572846 (2021).

62. Yang, K. et al. Self-healing, degradable, and implantable tissue-like sensor for monitoring of abnormal bladder activity. *Biosens. Bioelectron.* **288**, 117767 (2025).
63. Shen, X. et al. Harness-inspired and fully implantable electronic system for real-time urine volume monitoring. *Cell Rep. Phys. Sci.* **5**, 102281 (2024).
64. Nishiguchi, J. et al. Suppression of detrusor overactivity in rats with bladder outlet obstruction by a type 4 phosphodiesterase inhibitor. *BJU Int.* **99**, 680–686 (2007).
65. Tanaka, H., Kakizaki, H., Shibata, T., Mitsui, T. & Koyanagi, T. Effect of preemptive treatment of capsaicin or resiniferatoxin on the development of pre-micturition contractions after partial urethral obstruction in the rat. *J. Urol.* **170**, 1022–1026 (2003).
66. Çetinel, Ş, Çanıllıoğlu, Y. E., Çikler, E., Şener, G. & Ercan, F. Leukotriene D4 receptor antagonist montelukast alleviates protamine sulphate-induced changes in rat urinary bladder. *BJU Int.* **107**, 1320–1325 (2011).

Acknowledgements

This work is supported by the National Key Research and Development Program of China (2023YFC2414500 [Z.Y.L.], 2023YFC2414501 [Z.Y.L.], 2023YFC2414502 [F.H.]), the Guangdong Basic and Applied Basic Research Foundation (2021A1515110879 [Q.S.L.], 2023A1515011160 [Q.S.L.]), the National Natural Science Foundation of China (52473269 [Z.Y.L.], 62201558 [F.H.], 62201559 [Q.S.L.], 62471462 [Q.T.], 81970661 [B.K.S.], 82170790 [B.K.S.]), the Strategic Priority Research Program of the Chinese Academy of Sciences (XDB0930000 [Z.Y.L.]), the International Partnership Program of Chinese Academy of Sciences (Grant No. 321GJHZ2024176MI [Z.Y.L.]), the Guangdong Provincial Key Laboratory of Multimodality Non-Invasive Brain-Computer Interfaces (Grant no. 2024B1212010010 [Z.Y.L.]), the Shenzhen Basic Research Key Project (JCYJ20241202124919027 [Z.Y.L.]), the Shenzhen Science and Technology Program (JCYJ20230807140606012 [Q.S.L.]), the Shenzhen Science and Technology Program (KJZD20230923114108015 [F.H.]), the Shenzhen Science and Technology Program (grant no. KQTD20210811090217009 [Z.Y.L.]), the Shenzhen Engineering Research Center (XMHT20230115002 [Z.Y.L.]); the Clinical Research Project of Shandong University (2020SDUCRCC021 [Y.L.]), the Fundamental Research Funds for the Central Universities(2022JC004 [Y.L.]). Thank you to Dr. Qingsong Li and Dr. Qiong Tian for their technical, instrument, and reagent support.

Author contributions

H.F.L. and S.W. contributed equally to this work. H.F.L. and Z.Y.L. conceived the idea and designed the project. H.F.L., S.W., and Q.H.Y.Y. performed the experiments and analyzed the results. Z.C.T., Z.J.F., C.X.W., and J.Z. designed and conducted the theoretical calculations. H.Z., Z.C.T., L.C.L., F.H., R.F.Y., Y.Z., Z.J.F., L.P.C., Y.X.L., J.F.C., B.K.S., G.L.L., C.X.W., and J.Z. assisted with the figure production and experimental design. H.F.L. and S.W. wrote the manuscript. K.K.S., Y.L., and Z.Y.L. corrected the manuscript and supervised the whole project. All authors discussed the results and commented on the manuscript.

Competing interests

H.F.L. and Z.Y.L. are inventors on a Chinese patent application (No. CN202311855354.X). The remaining authors declare no competing interests.

Additional information

Supplementary information The online version contains supplementary material available at https://doi.org/10.1038/s41467-026-70680-0.

Correspondence and requests for materials should be addressed to Kaikai Song, Yan Li or Zhiyuan Liu.

Peer review information *Nature Communications* thanks Pedro Alpuim, who co-reviewed with Elisabete Fernandes, Sung-Min Park, and the other, anonymous, reviewer(s) for their contribution to the peer review of this work. A peer review file is available.